RSC Advances

RSC Advances

www.rsc.org/advances

ROYAL SOCIETY OF CHEMISTRY

www.rsc.org/advances

Journal Name

Dynamic Article Links ▶

ARTICLE TYPE

Tunable 3D hierarchical graphene/BiOI nanoarchitectures: *in situ* preparation and highly improved photocatalytic performance and photoelectrochemical properties under visible light irradiation

₅ **Hongwei Huang∗, Kun Liu, Yinglei Zhang, Kai Chen, Yihe Zhang∗, Na Tian**

Novel 3D hierarchical graphene/BiOI (GR-BiOI) nanoarchitectures have been successfully fabricated via
₁₀ an *in situ* self-assembly approach for the first time. More attractively, the hierarchical nanoarchitectures
can be adjusted by simply controlling the amount of grapheme oxide, which determines the improved
level of photocatalytic performance. The photochemical measurements revealed that the as-obtained 5%
GR-BiOI composite exhibits the most significantly enhanced photocatalytic activities for degradation of
Rhodamine B (RhB) and photocurrent (PC) generation under visible light irradiation ($\lambda > 420$ nm). This
₁₅ remarkably improved photocatalytic performance of GR-BiOI should be attributed to the well-
established interfacial interaction between graphene and BiOI, which can greatly facilitate the separation
and easy transfer of photogenerated electrons and holes to generate abundant $\bullet O_2^-$ and $\bullet OH$ active species
with powerful oxidability. It was verified by the photoluminescence (PL) spectra, electrochemical
impedance spectra (EIS), active species trapping and $\bullet O_2^-$ and $\bullet OH$ quantification experiments. Our work
₂₀ provides a new strategy for construction of hierarchical nanoarchitectures of high-performance composite
photocatalysts and paves an alternative way to the design and synthesis of graphene-based composites
aiming at special applications.

1. Introduction

Over decades, semiconductor photocatalysis is expected to be a
₂₅ very promising and green technology for environmental
remediation and energy conversion.[1-3] As a new type of
photocatalytic materials, bismuth compounds including $BiVO_4$,[4]
Bi_2MoO_6,[5] Bi_2WO_6,[6] Bi_2SiO_5,[7] $BiPO_4$,[8] BiOX (X=Cl, Br, I)[9,10]
and other new Bi-based photocatalyst[11-15] have drawn
₃₀ considerable attention for the promising practical industrial
application due to their high activity, high stability and
nontoxicity. Generally, Bi-based oxide semiconductors possess
the hybridized valence band (VB) by O 2p and Bi 6s, which can
effectively narrow the band gap and make them harvest more
₃₅ light with long wavelength.[16]

BiOX (X=Cl, Br, I) with the simplest Sillén structure featuring
its active $(Bi_2O_2)^{2+}$ layers and intergrown single halogen layers
exhibits the excellent photooxidation ability and interesting
structure-property relationship.[9,10] Especially, BiOI with a narrow
₄₀ band gap (Eg = 1.72-1.92 eV), responding to most of the visible
light, is a very valuable photocatalyst from the point of view of
utilizing solar energy.[17] Nevertheless, there are also some
drawbacks in the use of individual BiOI, e.g. high recombination
of photoinduced electron-hole pairs. Therefore, some
₄₅ modifications have been made to increase the lifetime of
photogenerated charge carriers of BiOI and obtain more

satisfying photocatalytic performance. These methods mainly
include BiOI self doping,[18] and BiOI-based heterojunctions, such
as $TiO_2/BiOI$,[19] $ZnO/BiOI$,[20] $BiPO_4/BiOI$,[21] $Bi_2O_3/BiOI$[22],
₅₀ $BiOCl/BiOI$,[23] $BiOBr/BiOI$,[24,25] et al. On the other hand, a two-
dimensional (2D) hybridized semiconductor graphene (GR) with
a conjugative π structure material has received ever-increasing
attention for their fascinating structural and electronic
properties.[26] Owing to its excellent conductivity, GR has been
₅₅ proved to be effective for reducing the recombination of the
photoinduced charge carriers and enhancing the photocatalytic
activity. The graphene-based composites, including TiO_2/GR,[27]
ZnO/GR,[28] $ZnWO_4/GR$,[29] $BiOCl/GR$[30] and $BiOBr/GR$[31,32] all
exhibits obvious enhancement of photocatalytic activity
₆₀ compared to bared samples. Nevertheless, most of the above GR-
based composites were synthesized by the solution-mixing
method, which provides much less intimate interfacial contact
than the approaches of *in situ* crystallization and *ex situ*
hybridization.[33]

₆₅ Currently, fabrication a high-performance photocatalyst
system via a facile and efficient route becomes the focus of
photocatalytic material design. Especially, it is very hard to
achieve the controllable synthesis of 3D hierarchical
nanoarchitectures with tunability. Conventional methods always
₇₀ suffer from high temperature and pressure, long reaction times,

special capping agents (like surfactants) and high cost. Thus, a simple and efficient approach to fabrication of a high-performance photocatalyst system with 3D hierarchical nanoarchitectures is challenging and highly desirable.

Herein, we demonstrate for the first time a facile, fast and efficient ethylene glycol (EG) assisted approach for preparing hierarchical GR-BiOI nanoarchitectures. It is interesting to find that the assembly mode of BiOI flowers on GR varied with the change of GR content. The photochemical properties of GR-BiOI composites were demonstrated by photodecomposition of rhodamine B (RhB) and photocurrent (PC) measurements under visible light irradiation ($\lambda > 420$ nm). In particular, the possible mechanisms for the remarkably improved photocatalytic performance were systematically investigated based on the results of photoluminescence (PL) emission spectra, electrochemical impedance spectra (EIS), active species trapping and $\bullet O_2^-$ and $\bullet OH$ quantification experiments.

2. Experimental Section

2.1 Synthesis

All chemicals were analytical reagent grade and were used without further purification. Graphene oxide (GO) was synthesized from natural graphite powders by a modified Hummers' method.[34]
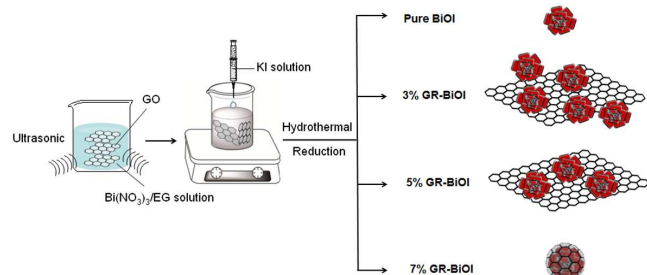
Scheme 1. Schematic illustration of the preparation of the GR-BiOI nanocomposites.

GR-BiOI composites were synthesized by an *in situ* crystallization method as illustrated in Scheme 1. Different amounts of as-prepared GO and 1mmol of $Bi(NO_3)_3 \cdot 5H_2O$ were ultrasonically dispersed into 20 mL ethylene glycol. 1mmol KI was dissolved in 20 mL deionized water, and then added drop wise into the above GO and $Bi(NO_3)_3 \cdot 5H_2O$ suspension under strong magnetic stirring. Subsequently, the suspension was stirred for 10 min at room temperature. After that, the suspension was transferred into a 100 mL Teflon-lined stainless autoclave and heated at 120 °C for 10 min to reduce GO. After cooling, the products were filtered, washed with deionized water and ethanol for several times and dried at 60 °C for 12 h. The mass fractions of GO 1%, 3%, 5% and 7% were donated as 1%, 3%, 5% and 7% GR-BiOI, respectively. For reference, pure BiOI was prepared under the same conditions without adding GO.

2.2 Characterization

A D8 Advance X-ray diffractometer (Bruker AXS, Germany) with Cu Kα radiation was employed to analyse the crystal structures of the obtained samples. The FTIR spectra of the as-obtained samples were recorded on a PerkinElmer Spectrum 100 FTIR spectrophotometer in the 4000~400 cm^{-1} range. The

morphology and microstructure of the products were investigated by a S-4800 scanning electron microscope (SEM). Transmission electron microscopy (TEM) and high-resolution transmission electron microscopy (HRTEM) images were obtained by using a JEM-2100 electron microscopy (JEOL, Japan). Specific surface areas of samples were characterized by the nitrogen adsorption BET method with a Micromeritics 3020 instrument. UV-vis diffuse reflectance spectra (DRS) were recorded from PerkinElmer Lambda 35 UV–vis spectrometer. The spectra were collected at 200–1000 nm referenced to $BaSO_4$. Room temperature emission spectra were measured on a Hitachi F-4600 fluorescence spectrophotometer with a 150 W Xenon lamp as the excitation lamp.

2.3 Photocatalytic activity experiment.

The photocatalytic activity of GR-BiOI composites were evaluated by photodegradation of the organic dyes (rhodamine B) RhB under visible light with a xenon lamp coupled with 420 nm filters ($\lambda > 420$ nm, 1000 W). 0.05g of as-prepared GR-BiOI or pure samples was dispersed into 50 mL of $3*10^{-5}$ mol/L RhB solution. First, the reaction mixture was stirred in dark for 2 h to ensure complete adsorption-desorption equilibrium of the organic dye by the catalyst. After that, about 3 mL of the suspension was taken at certain intervals under irradiation, and then separated through centrifugation. The concentration of RhB was determined by recording the absorption spectra of residual dye by UV−vis spectroscopy based on the absorbance at 553 nm.

2.4 Active species trapping and $\bullet O^{2-}$ and $\bullet OH^-$ quantification experiments.

For detecting the active species in the photocatalytic system, 1 mM ethylenediaminetetraacetic acid disodium salt (EDTA-2Na), 1 mM benzoquinone (BQ) and 1.0 mM iso-propanol (IPA) were added as the active species quenchers of holes (h$^+$), $\bullet O_2^-$ and $\bullet OH$, respectively.[35,36] The method was similar to the former photocatalytic activity experiment. In order to determine the amount of $\bullet O_2^-$ generated from the potocatalytic system, 0.025 mM nitroblue tetrazolium (NBT), which exhibits an absorption maximum at 259 nm and can react with $\bullet O_2^-$, was utilized.[37] The production of $\bullet O_2^-$ was quantitatively analyzed through recording the concentration of NBT with an UV−vis spectrophotometer. Moreover, to estimate the relative concentration of hydroxyl radicals ($\bullet OH$ radicals), the terephthalic acid (TA) fluorescence method was utilized, because it can react readily with $\bullet OH$ to produce a highly fluorescent 2-hydroxyterephthalic acid.[36] The production of $\bullet OH$ generated from BiOI and GR-BiOI was quantitatively analyzed by detecting the concentration of 2-hydroxyterephthalic acid on a Hitachi F-4600 fluorescence spectrophotometer at 425 nm with the excitation wavelength of 315 nm. The NBT transformation and TA-PL methods were also similar to the former photocatalytic activity test and above active species trapping with NBT and TA replacing the RhB.

2.5 Photoelectrochemical measurements.

The photoelectrochemical tests were carried out in a three-electrode system with a 0.1 M Na_2SO_4 electrolyte solution by using an electrochemical system (CHI-660B, China). Platinum wire and saturated calomel electrodes (SCE) were used as the counter electrode and reference electrode, respectively. GR-BiOI

and pure BiOI film electrodes on ITO served as the working electrode. The intensity of light was 1 mW/cm^2. The photocurrent (PC) generation and electrochemical impedance spectra (EIS) with visible light on and off were measured at 0.0 V. A 5 mV
5 sinusoidal ac perturbation was applied to the electrode.

3. Results and discussion

3.1 Morphological structure

The morphologies and microstructures of BiOI, GR and GR-BiOI hybrid composites were obtained by scanning electron
10 microscopy (SEM). Fig. 1a and 1b shows the SEM images of pure BiOI and GR, respectively. It is very important to notice that the as-prepared BiOI exhibits a 3D hierarchical flower-like morphology, which is assembled by numerous BiOI nanosheets. The diameters of the entire BiOI micro-flowers are about 2 μm.
15 After graphene was introduced into the BiOI self-assembly system, the assembly mode of GR and BiOI are found varying with their proportions. Fig. 1c and 1d presented the 1% and 3% GR-BiOI composites, respectively. It can be seen that only partial BiOI microspheres equipped on the surface of GR as GR was in
20 low content. When the content of GR increased to 5%, the flower-like BiOI products were all uniformly assembled on the surface of GR, as shown in Fig. 1e and 1f. As a result, the perfect 3D self-assembled hierarchical graphene/BiOI nanoarchitectures were obtained. Moreover, another interesting phenomenon
25 observed was that graphene-wrapped BiOI can also be obtained as the GR content reaches 7%. As shown in Fig. 1g and 1h, most of BiOI micro-flowers were well-encapsulated in the GR sheets. It can be inferred that *in situ* synthesis is conducive to intimate interfacial contact between flower-like BiOI and GR.
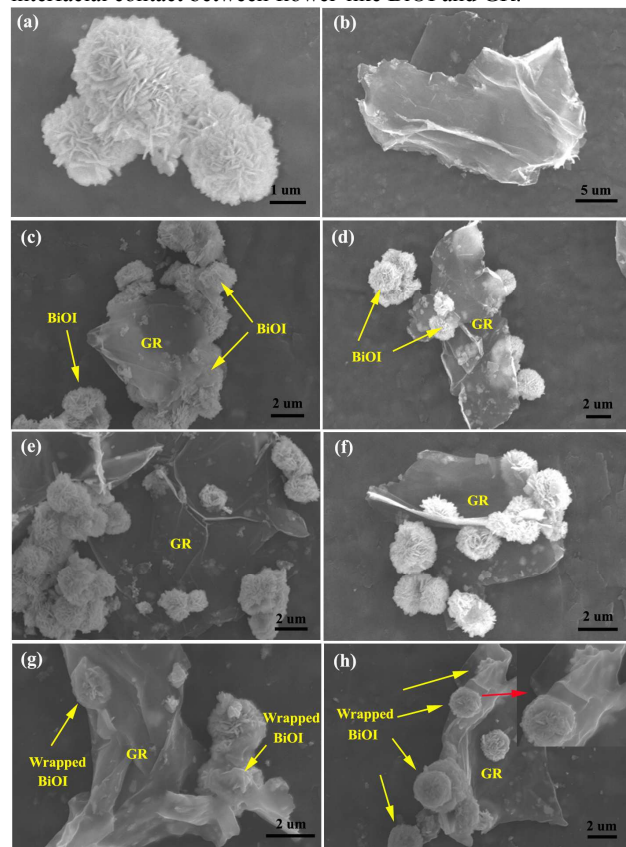

Fig. 1 SEM images of as-prepared (a) pure BiOI, (b) graphene and GR-BiOI composites with GR amount of (c) 1%, (d)3%, (e,f) 5% and (g,h) 7%.

The pure BiOI, GR and GR-BiOI composites were further characterized by TEM and HRTEM. As presented in Fig. 2a, the
35 as-prepared BiOI micro-flowers are constructed by large number of nanoplates and the average thicknesses of these nanoplates are about 20-40 nm. Fig. 2c confirmed the 3D hierarchical nanoarchitectures of 5% GR-BiOI composites, in which the BiOI micro-flower was firmly assembled on the surface of GR. The
40 contact interface between BiOI and GR can also be clearly seen. Compared with GO-BiOI (Fig. S1), obviously the hydrothemal process did not alter the morphology of the nanocomposites. Fig. 2d is the TEM image of 7% GR-BiOI. It is obvious to see that the BiOI micro-flower is completely enwrapped by GR, which
45 indicated that the self assambly of BiOI micro-flower took place in the space between graphene layers with high graphene content. In Fig. 2e and 2f, the high-resolution transmission electron microscopy (HRTEM) image shows the characteristic lattice fringes of BiOI nanoplates in the composites. In order to obtain
50 clearer lattice fringe, fast Fourier transform (FFT) images (Fig. 2g and Fig. 2i) and reduced FFT images (Fig. 2h and Fig. 2j) were obtained. The interplanar instance resolved from lattice fringe is 0.301 and 0.281 nm (as seen in Fig. 2h and 2j, respectively), which is consistent with the spacing of the
55 corresponding (102) and (110) planes of tetragonal phase of BiOI. It was also confirmed by the following XRD results.
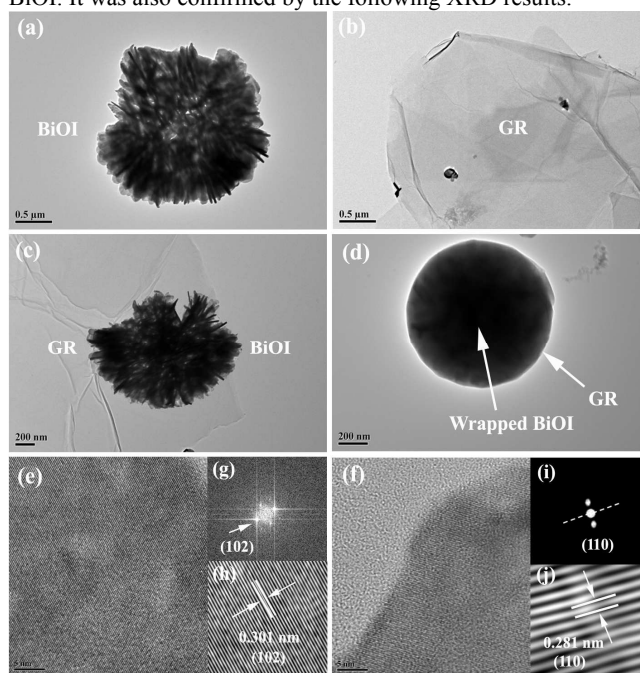

Fig. 2 TEM images of (a) pure BiOI, (b) graphene, (c) 5% GR-BiOI (d) 7% GR-BiOI, (e,f) HRTEM images (g, i) FFT (fast Fourier transition) patterns and
60 (h, j) inverse FFT (fast Fourier transition) patterns of the lattice fringe of BiOI.

3.2 Crystal structure and phase analysis.

Fig. 3 shows the crystal structure of BiOI along the *a-c* and *a-b* planes. Tetragonal phase BiOI possesses a Sillén structure with
65 typically layered configuration, which is composed of $[Bi_2O_2]^{2+}$ layers and I$^-$ ions between them. Its space group is *P4/nmm*(129) with cell parameters a=4.0900 Å and c=7.2100 Å. The

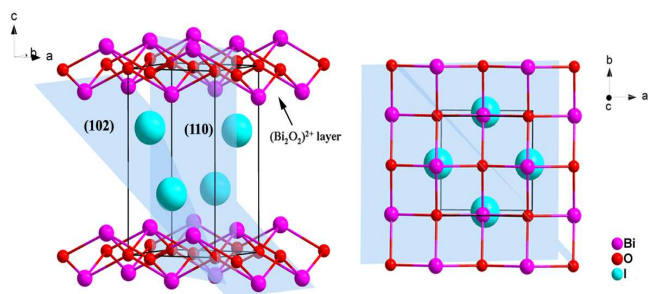corresponding (102) and (110) crystal faces were also highlighted.

Fig. 3 Crystal structure of BiOI along a-c and a-b plane (110 and 102 planes are highlighted).
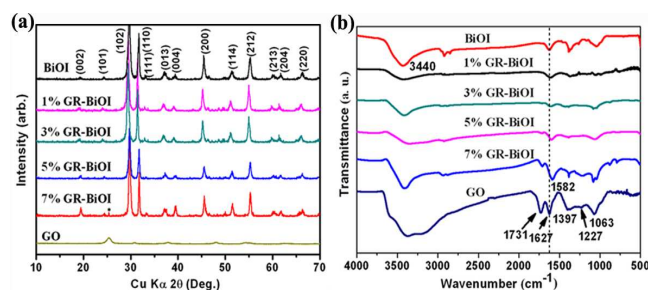

Fig. 4 (a) XRD patterns and (b) IR sepctra of pure BiOI and GR-BiOI composites.

The crystal structure and crystallization phases of the products were characterized by the X-ray powder diffraction (XRD). Fig. 4a presents the XRD patterns of BiOI, graphene oxide (GO) and GR-BiOI composites. The pure BiOI displays a series of neat diffraction peaks with high purity and crystallinity, which can be indexed into the tetragonal phase of BiOI (JCPDS 10-0445). Similar with those in other graphene composites, the characteristic diffraction peaks of GO and GR were all invisible due to the destruction of regular stacking of GO by the reduction process under hydrothermal conditions and the low amount and intensity of graphene in the composite.[35-37]

3.3 Chemical composition.

Fig. 4b shows a comparison of the FTIR spectra of pure BiOI, GO and GR-BiOI composites. The characteristic peaks of GR are verified by the bands at 1731 cm^{-1}, 1727 cm^{-1}, 1397 cm^{-1}, 1227cm^{-1} and 1063 cm^{-1}, which refers to the C=O stretching vibration of COOH groups, skeletal vibrations of unoxidized graphitic domains, O-H deformation vibration of the C-OH groups, the epoxy C-OH stretching vibration and C-O-C stretching vibrations, providing the evidence for the presence of different types of oxygen-containing functional groups including –COOH, -C-OH, -C=O and –C-O-C on the graphite oxide.[38] For pure BiOI, the peaks at 3440 cm^{-1} and 1630 cm^{-1} should originate from the absorption of water or O-H groups.[39] The IR peak observed at 1385 cm^{-1} results from the OH absorption of hydrogen-related defects.[40] In the case of the GR–BiOI composites, the characteristic peaks of GO become weaker in intensity or even disappear compared with that of the pure GO, demonstrating that the oxygenous functional groups attached to the basal GO layers have been removed after the hydrothermal treatment process. The peak intensity at 1385 cm^{-1} in GR-BiOI composites dramatically decreased, indicating that defect sites of BiOI may be occupied by graphene. In addition, a new absorption band at 1582 cm^{-1}, attributing to the skeletal vibration of the aromatic -C=C- bonds of the graphene network has been observed and gradually increased in intensity with the increase of GR loading content.[41] Compared with pure GO and BiOI, the 7% GR-BiOI shows a much broader peak around 1227 cm^{-1}. This enhanced C−OH stretching interaction may indicate that the graphene and BiOI are chemically bonded.[34]

3.4 Optical property.

The ultraviolet-visible diffuse reflectance spectra of pure BiOI and GR-BiOI composites were shown in Fig. 5a. Compared to pure BiOI with an absorption edge 690nm, all the GR-BiOI composites exhibit obvious enhancement on the visible-light absorption. In semiconductors, different optical transitions can result in different types of band gap. The band gap (E_g) can be determined by the Kubelka–Munk function[9,42,43]:

$$\alpha h\nu = A (h\nu – E_g)^{n/2} \tag{1}$$

Where α, h, ν, E_g and A are absorption coefficient, Planck constant, light frequency, band gap energy, and a constant, respectively. Among them, n is determined by the type of optical transition of a semiconductor (n = 1 for direct transition and n = 4 for indirect transition). For BiOI, the n value is 4. The indirect band gaps estimated from the Kubelka–Munk function (Fig. 5b) are calculated to be 1.72, 1.42, 1.22, 1.11 and 1.07 for BiOI, 1%, 3%, 5% and 7% GR-BiOI, respectively. The optical results indicated that the incorporation of GR into BiOI effectively narrow the band gap from the valence band to conduction band.
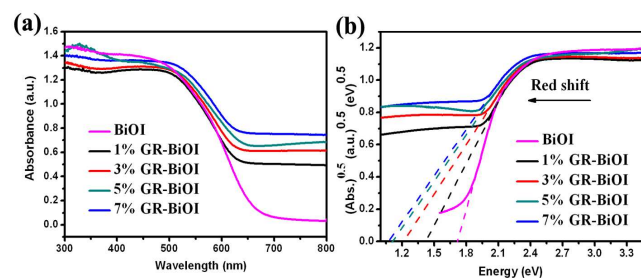

Fig. 5 (a) UV-vis diffuse reflectance spectra and (b) the band gap energies of pure BiOI, 1%, 3%, 5% and 7% GR-BiOI composites.

3.5 Photocatalytic activity under visible light irradiation.

The photocatalytic performance of the as-prepared pure BiOI and GR-BiOI composite photocatalysts was evaluated by degradation of RhB molecules in aqueous solution under visible light irradiation (λ > 420 nm) as shown in Fig. 6. The photodegradation curves with error bars were also presented in Fig. S2. As displayed in Fig. 6a, the pure BiOI shows relatively poor activity, and only 20% RhB was degraded under visible light for 4h. Comparatively, the degradation efficiencies were 34%, 39%, 76% and 70% for 1% GR-BiOI, 3% GR-BiOI, 5% GR-BiOI and 7% GR-BiOI, respectively within the same

irradiation time. It can be seen that the photocatalytic activity gradually increased as increasing the loading content of graphene. Nevertheless, the photocatalytic activity was decreased when the content of graphene reached 7%. As shown in Fig. 6a, the single GR almost has no photodegradation effect on RhB. With the further increase of GR content to 7%, most of BiOI microspheres were covered or wrapped by graphene as shown in Fig. 1g and h, which lead to a largely reduced visible-light absorption of BiOI. Hence, the amount of photoexcited electron-hole pairs occurred in BiOI in 7% GR-BiOI composite was also decreased. As a result, the 5% GR-BiOI possesses the most improved photocatalytic performance, with a RhB degradation efficiency of approximately 80%.
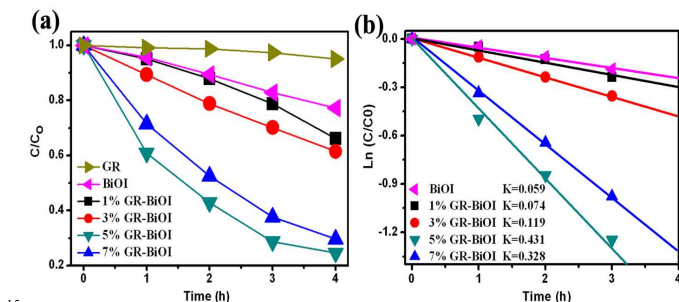

Fig. 6 (a) Photocatalytic degradation curves of RhB over GR, pure BiOI, 1%, 3%, 5% and 7% GR-BiOI composites under the irradiation of visible light ($\lambda >$ 420 nm). (b) Apparent rate constants for the photodegradation of RhB.

In order to quantitatively understand the reaction kinetics of the photocatalytic degradation process of RhB, the apparent pseudo-first-order model according to the Langmuir-Hinshelwood (L-H) kinetics model was applied, as expressed by the following equation[12,13]:

$$Ln (C_0/C) = k_{app}t \qquad (2)$$

where k_{app} is the apparent pseudo-first-order rate constant (h^{-1}), C_0 is initial RhB concentration (mol/L), C is RhB concentration in aqueous solution at time t (mol/L). It can be found that there is a good correlation to the pseudo-first-order model. As shown in Fig. 6b, the apparent rate constant k is 0.059 h^{-1}, 0.074 min^{-1}, 0.119 h^{-1}, 0.431 h^{-1} and 0.328 h^{-1} for the pure BiOI, 1% GR-BiOI, 3% GR-BiOI, 5% GR-BiOI and 7% GR-BiOI, respectively. Thus, the optimized photocatalytic efficiency was obtained in 5% GR-BiOI, which is about 7.3 times higher than that of pure BiOI. As the specific surface area of a photocatalyst is closely related to its photocatalytic activity, the BET surface areas of the pristine BiOI, 1% GR-BiOI, 3% GR-BiOI, 5% GR-BiOI and 7% GR-BiOI composites were measured, and their values are 8.34, 9.82, 13.64, 19.57 and 27.68 m^2/g, respectively. The comparisons between our photocatalysts on "same surface area" basis were also performed. The apparent rate constants per surface areas were 0.0071, 0.0075, 0.0087, 0.0220 and 0.0119 (h•m^2/g)$^{-1}$ for BiOI, 1% GR-BiOI, 3% GR-BiOI, 5% GR-BiOI and 7% GR-BiOI, respectively. The 5% GR-BiOI still possesses the highest photocatalytic efficiency, which is approximately 3.1 times higher than that of pure BiOI.

3.6 Investigation on photocatalytic mechanism.

As photoluminescence (PL) emission spectra mainly result from the recombination of free carriers, therefore, PL spectra can be employed to survey the separation efficiency of the photogenerated electrons and holes in a semiconductor.[12,44] Generally, lower PL irradiance reflects the lower recombination of the charge carriers, which results in higher photocatalytic activity. Fig. 7 depicts the PL spectra of BiOI and GR-BiOI composites at room temperature. From the figure, the highest and lowest emission intensities were observed in pure BiOI and 5% GR-BiOI, respectively. Thus, the lowest recombination of photogenerated electrons and holes occurred in 5% GR-BiOI, which is in good agreement with the result from photodegradation experiment.
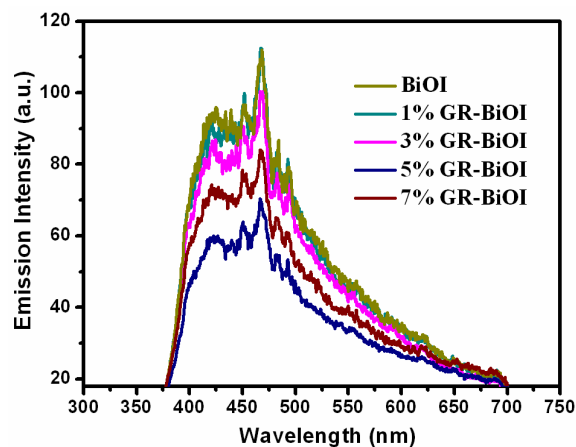

Fig. 7 PL spectra of over pure BiOI and GR-BiOI composites.

The photocurrent-time responds, which may directly correlate with the recombination efficiency of the photogenerated carriers, were utilized to investigate the interfacial charge transfer dynamics of BiOI and GR-BiOI.[45] As shown in Fig. 8a, the photocurrent generation with good reproducibility for the two samples can be observed under visible light irradiation, indicating that the electrodes are stable and the photoresponses is quite reversible. The much larger photocurrent density observed in GR-BiOI is 6 times that of pristine BiOI, which is in good agreement with the photodegradation tests. This result reflects the more efficient transfer of photoinduced charge carriers of GR-BiOI composite owing to the interfacial interaction between BiOI and graphene.

The migration and transfer processes of photogenerated electron-hole pairs in semiconductors can also be elucidated by the electrochemical impedance spectra (EIS) Nyquist plots.[13] The smaller arc diameter in Nyquist plots implies a lower resistance of the interfacial charge transfer in the electrode-electrolyte interface region on the surface of electrode. As shown in Fig. 8b, the 5% GR-BiOI exhibits a significantly smaller arc diameter in EIS compared to BiOI, indicating a more effective separation of photogenerated electron-hole pairs and fast interface charge transfer occurred in GR-BiOI composite.
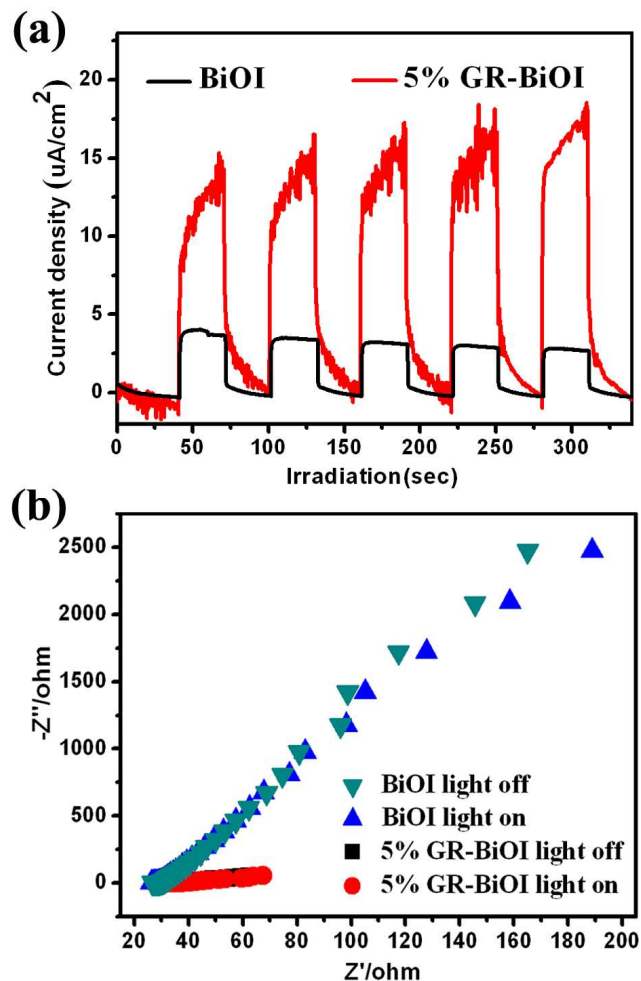
Fig. 8 (a) Comparison of transient photocurrent response and (b) EIS Nynquist plots of of pure BiOI and 5% GR-BiOI composite with light on/off cycles under the irradiation of visible-light irradiation (λ > 420 nm, [Na₂SO₄] = 0.1 M).

To reveal the photocatalytic mechanism in the degradation process over GR-BiOI composite, the active species trapping experiments were performed. The sacrificial agents, including 1, 4-benzoquinone (BQ), disodium ethylenediaminetetraacetate (EDTA) and iso-propanol (IPA) were used as the scavengers of superoxide radical ($\cdot O_2^-$), hole (h^+) and hydroxyl radical ($\cdot OH$), respectively.[35,36] As shown in Fig. 9, 1 mM of EDTA (a hole scavenger) almost has no effect on the photocatalytic activity of GR-BiOI, indicating that very few of the holes (h^+) were involved in the degradation of RhB. Conversely, the degradation rate for RhB was significantly depressed with the addition of 1 mM of $\cdot O_2^-$ scavenger BQ, demonstrating the existence of abundant $\cdot O_2^-$ radical species. In addition, obvious decrease of degradation rate was also observed when 1 mM of tertbutyl alcohol (TBA) as a scavenger for $\cdot OH$ radical species was added, suggesting that the $\cdot OH$ pathways also have a crucial role in the process of RhB photooxidation. It indicated that, in our photocatalyst systems, the holes are easier to be transformed to $\cdot OH$ radicals than reaction with RhB or scavengers. Thus, the $\cdot O_2^-$ and $\cdot OH$ are the two main active species in the degradation process of RhB over GR-BiOI composite.
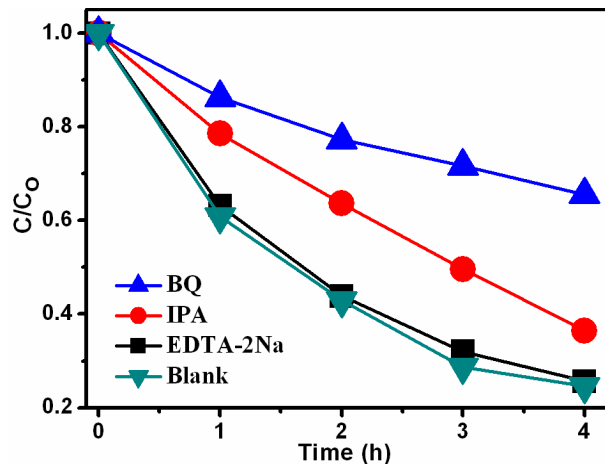

Fig. 9 (a) Photodegradation of RhB over 5% GR-BiOI composite in the presence of different scavengers.
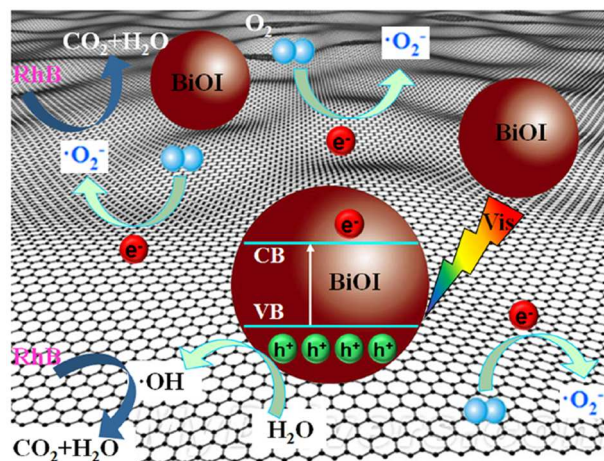

Fig. 10 Schematic diagram of GR-BiOI composite under visible light irradiation.

Accordingly, the possible photocatalytic mechanism of GR-BiOI composite was proposed as depicted in Fig. 10. Under visible light irradiation, the separation of electron and hole pairs occurred, and the electrons were injected into the conduction band of BiOI. Due to the strong interfacial interaction between BiOI micro-flowers and graphene originated from *in situ* crystallization, the photogenerated electrons are very easy to transfer from the conduction band of BiOI onto the surface of graphene. As we all know, graphene possesses a two-dimensional conjugated π structure and superior electrical conductivity. Thus, graphene can serve as an acceptor of the photogenerated electrons of BiOI in the GR-BiOI composites. These electrons further react with O_2 adsorbed on the surface of graphene to generate abundant $\cdot O_2^-$, which play a crucial role in photooxidation of RhB. On the other hand, the holes left in the VB of BiOI can oxidize the OH^- ions in solution to produce active $\cdot OH$ radicals with powerful oxidization. Therefore, the 3D self-assembled hierarchical graphene/BiOI nanoarchitectures could greatly facilitate the separation of photogenerated charge carriers and effectively suppress the recombination of electrons and holes, leaving more $\cdot O_2^-$ and $\cdot OH$ radicals as active species for high efficient photooxidation degradation of RhB. Furthermore, the

incorporation of graphene can enhance the surface absorption ability of photocatalyst system, which is also beneficial for the photocatalytic reaction as it is essentially a two-steps process, surface absorption and photooxidation.
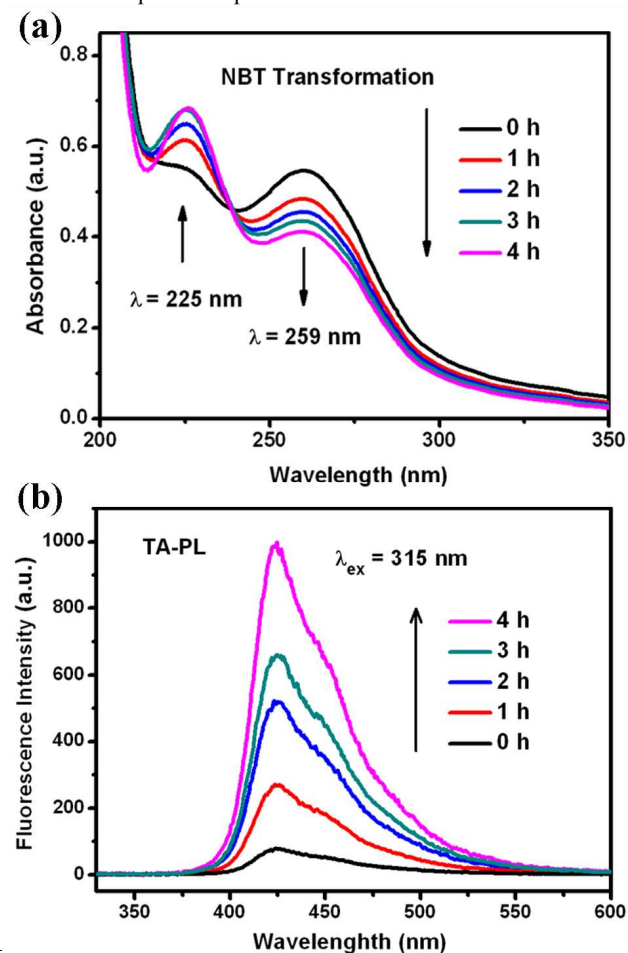

Fig. 11 (a) Absorption spectra of NBT and (b) Fluorescence spectra of a TAOH solution over 5% GR-BiOI composite with 4 h visible light irradiation (λ > 420 nm).

In order to further confirm the supposed photocatalytic mechanism and verify the contribution of $\cdot O_2^-$ and $\cdot OH$ radicals, quantification experiments of $\cdot O_2^-$ and $\cdot OH$ production over GR-BiOI were performed. Fig. 11a presents the absorption spectra centered at 259 nm of NBT (detection agent of $\cdot O_2^-$ production) with 4 h visible light irradiation (λ > 420 nm) during the photocatalytic reaction. It can be found that the characteristic absorption peak at 259 nm of NBT obviously decreased with the increase of irradiation time, indicating NBT was transformed by abundant $\cdot O_2^-$ radicals generated from GR-BiOI photocatalyst system.[37] It further revealed that in GR-BiOI composite, the photogenerated electrons on BiOI could easily transfer to graphene, leading more photogenerated electrons react with O_2 to produce $\cdot O_2^-$ and take part in decomposition of RhB. Moreover, terephthalic acid photoluminescence probing technique (TA-PL) was also utilized to detect the $\cdot OH$ radicals because TA can react with $\cdot OH$ radicals to form highly fluorescent 2-hydroxyterephthalic acid (TAOH). As revealed in Fig. 11b, the emission irradiance of TAOH dramatically increased as

prolonging the irradiation time, which demonstrated that the $\cdot OH$ species play an important role in the photocatalytic reaction over GR-BiOI composite. These results further confirmed that the self-assembled hierarchical GR/BiOI nanoarchitecture photocatalyst system can indeed facilitate the separation of photogenerated charge carriers greatly, thus to generate large number of $\cdot O_2^-$ and $\cdot OH$ species with powerful oxidability for highly efficient photocatalytic activity.

Conclusions

In summary, we have successfully developed a very simple *in situ* self-assembly method by using ethylene glycol as chelating agent for construction of tunable 3D hierarchical graphene/BiOI (GR-BiOI) nanoarchitectures for the first time. It is found that the BiOI micro-flowers can be not only assembled on the surface of graphene, but also totally wrapped by graphene sheets. All the GR-BiOI composites were found to exhibit much higher photocatalytic efficiency than pure BiOI visible light irradiation (λ > 420 nm). The optimum photocatalytic activity, obtained in 5% GR-BiOI with perfect surface-equipped configuration, is about 7.3 and 6 times higher than those of pure BiOI for photodecomposition of RhB and photocurrent generation, respectively. The significantly improved photocatalytic performance has been demonstrated to be due to the high separation efficiency of photogenerated charge carriers originated from the well-established interfacial interaction between graphene and BiOI, as revealed in the PL and EIS tests. The active species trapping and quantification experiments indicated $\cdot O_2^-$ and $\cdot OH$ play crucial roles in photooxidation degradation reaction, which further confirmed the high separation efficiency of photogenerated electrons and holes in GR-BiOI. This work may be a guide for fabricating other high-performance Bi-based composite-photocatalysts with hierarchical nanoarchitectures and designing graphene-based composites aiming at special applications.

Acknowledgement

Notes and references

Beijing Key Laboratory of Minerals Materials and Utilization of Solid Waste,China University of Geosciences, Beijing, 100083, PR China, Tel: 86-10-82332247; E-mail: hhw@cugb.edu.cn; zyh@cugb.edu.cn.

1 L. Shang, T. Bian, B. Zhang, D. H. Zhang, L. Z. Wu, C. H. Tung, Y. D. Yin and T. R. Zhang *Angew. Chem. Int. Ed.,* 2014, **53,** 250-254.
2 A. Kubacka, M. Fernández-García and G. Colón. *Chem. Rev.,* 2011, **112,** 1555-1614
3 R. Asahi, T. Morikawa, T. Ohwaki, K. Aoki and Y. Taga. *Science.,* 2001, **293,** 269-271.
4 A. Kudo, K.. Omori and H. Kato. *J. Am. Chem. Soc.* 1999, **121,** 11459-11467.
5 J. Bi, L. Wu, J. Li, Z. Li, X. Wang and X. Fu, *Acta Mater.,* 2007, **55,** 4699-4705.
6 C. Zhang and Y. F. Zhu. *Chem. Mater.,* 2005, **17,** 3537-3545.

7 R. G. Chen, J. H. Bi, L. Wu, W. J. Wang, Z. H. Li and X. Z. Fu. *Inorg. Chem.,* 2009, **48,** 9072-9076.

8 C. S. Pan and Y. F. Zhu. *Environ. Sci. Technol.,* 2010, **44,** 5570−5574.

9 X. Zhang, Z. H. Ai, F. L. Jia and L. Z. Zhang, *J. Phys. Chem. C,* 2008, **112,** 747-753.

10 J. Henle, P. Simon, A. Frenzel, S. Scholz and S. Kaskel. *Chem. Mater.,* 2007, **19,** 366-373.

11 X. Xiao, C. L. Xing, G. P. He, X. X. Zuo, J. M. Nan and L. S. Wang. *Appl. Catal. B.,* 2014, **148,** 154-163

12 H. W. Huang, S. B. Wang, N. Tian and Y. H. Zhang. *RSC Adv.,* 2014, **4,** 5561-5567.

13 H. W. Huang, Y. He, Z. S. Lin, L. Kang and Y. H. Zhang. *J. Phys. Chem. C.,* 2013, **117,** 22986-22994.

14 H. W. Huang, Y. He, R. He. Z. S. Lin, Y. H. Zhang, S. C. Wang, *Inorg. Chem.,* 2014, **53,** 8114-8119.

15 H. W. Huang, K. Liu, K. Chen, Y. L. Zhang, Y. H. Zhang and S. C. Wang, *J. Phys. Chem. C,* 2014, **118,** 14379-14387.

16 J. W. Tang, Z. G. Zou and J. H. Ye. *J. Phys. Chem. C.,* 2007, **111,** 12779-12785.

17 X. Xiao and W. D. Zhang *J. Mater. Chem.,* 2010, **20,** 5866-5870.

18 X. Zhang and L. Z. Zhang. *J. Phys. Chem. C.,* 2010, **114,** 18198-18206

19 X. Zhang, L. Z. Zhang, T. F. Xie and D. J. Wang. *J. Phys. Chem. C.,* 2009, **113,** 7371-7378

20 J. Jiang, X. Zhang, P. B. Sun and L. Z. Zhang, *J. Phys. Chem. C.*, 2011, **115,** 20555-20564

21 J. Cao, B. Y. Xu, H. L. Lin and S. F. Chen, *Chem. Eur., J.,* 2013, **228,** 482-488.

22 Y. Y. Li, J. S. Wang, H. C. Yao, L. Y. Dang and Z. J. Li, *Catal. Commun.,* 2011, **12,** 660-664.

23 T. B. Li, G. Chen, C. Zhou, Z. Y. Shen, R. C. Jin and Sun, J. X. *Dalton Trans.,* 2011, **40,** 6751-6758

24 W. D. Wang, F. Q. Huang, X. P. Lin and J. H. Yang, *Catal. Commun.,* 2008, **9,** 8-12.

25 J. Cao, B. Y. Xu, B. D. Luo, H. L. Lin and S. F. Chen. *Catal. Commun.,* 2011, **13,** 63-68.

26 Y. Zhang, Y. Tan, H. L. Stormer and P. Kim. *Nature.,* 2005, **438,** 201-204.

27 Y. H. Zhang, Z. R. Tang, X. Z. Fu and Y. J. Xu. *ACS Nano.,* 2010, **4,** 7303-7314.

28 Q. Luo, X. Yu, B. Lei, H. Chen, D. Kuang and C. Su. *J. Phys. Chem. C.,* 2012, **116,** 8111-8117.

29 X. J. Bai, L. Wang and Y. F. Zhu. *ACS Catal.,* 2012, **2,** 2769-2778.

30 F. D. Gao, D. W. Zeng, Q. W. Huang, S. Q. Tian and C. S. Xie. *Phys. Chem. Chem. Phys.,* 2012, **14,** 10572-10578.

31 Z. H. Ai, W. K. Ho and S. C. Lee. *J. Phys. Chem. C.,* 2011, **115,** 25330-25337.

32 X. M. Zhang, X. F. Chang, M. A. Gondal, B. Zhang, Y. S. Liu and G. B. Jia. *Appl. Surf. Sci.,* 2012, **258,** 7826-7832.

33 X. Huang, X. Qi, F. Boey and H. Zhang, *Chem. Soc. Rev.,* 2012, **41,** 666-686.

34 W. S. Hummers and R. E. Offeman, *J. Am. Chem. Soc.,* 1958, **80,** 1339-1339.

35 L. Ye, J. Liu, C. Gong, L. Tian, T. Peng and L. Zan, *ACS Catal.,* 2012, **2,** 1677-1683.

36 X. J. Bai, L. Wang and Y. F. Zhu. *ACS Catal.,* 2012, **2,** 2769-2778.

37 L. Q. Ye, J. Y. Liu, Z. Jiang, T. Y. Peng and L. Zan. *Appl. Catal., B* 2013, **142,** 1-7.

38 T. F. Yeh, J. M. Syu, C. Cheng, T. H. Chang and H. Teng. *Adv. Funct. Mater.,* 2010, **20,** 2255-2262.

39 Q. J. Xiang, J. G. Yu and M. Jaroniec. *J. Phys. Chem. C.,* 2011, **115,** 7355-7363.

40 Z. S. Li, T. Yu, Z. G. Zou and J. H. Ye. *Appl. Phys. Lett.,* 2006, **88,** 071917-(1-3).

41 C. Nethravathi and M. Rajamathi. *Carbon.,* 2008, **46,** 1994-1998.

42 H. W. Huang, J. Y. Yao, Z. S. Lin, X. Y. Wang, R. He, W. J. Yao, N. X. Zhai and C. T. Chen, *Angew. Chem., Int. Ed.,* 2011, **50,** 9141.

43 H. W. Huang, L. J. Liu, S. F. Jin, W. J. Yao, Y. H. Zhang and C. T. Chen. *J. Am. Chem. Soc.,* 2013, **135,** 18319-18322.

44 X. J. Wang, Q. Wang, F. T. Li, W. Y. Yang, Y. Zhao, Y. J. Hao and S. J. Liu. *Chem. Eng. J.,* 2013, **234,** 361–371.

45 H. Kim, P. Borse, W. Choi and J. Lee. *Angew. Chem., Int. Ed.,* 2005, **44,** 4585-4589.

RSC Advances Accepted Manuscript

Table of contents entry
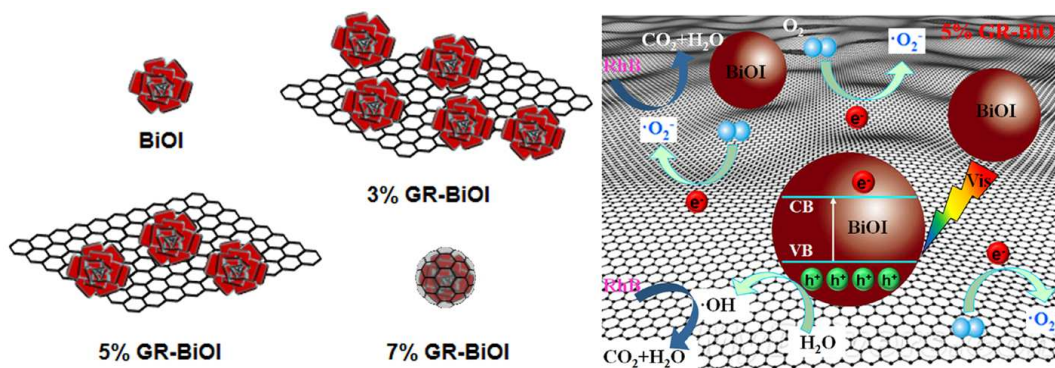
Tunable 3D hierarchical graphene/BiOI nanoarchitectures have been fabricated via a simple *in situ* self-assembly route. Based on the high efficient interfacial charge transfer between graphene and BiOI, their photochemical performance was significantly improved.